Additive Manufacturing 69 (2023) 103529

Contents lists available at ScienceDirect

Additive Manufacturing

journal homepage: www.elsevier.com/locate/addma

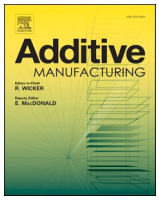

Strength-enhanced volume decomposition for multi-directional additive manufacturing

Danjie Bi [a], Molong Duan [a,b], Tak Yu Lau [a], Fubao Xie [c], Kai Tang [a,b,d,*]

[a] Department of Mechanical and Aerospace Engineering, Hong Kong University of Science and Technology, Hong Kong Special Administrative Region
[b] HKUST Shenzhen-Hong Kong Collaborative Innovation Research Institute, Futian, Shenzhen, China
[c] Research Institute of Aero-Engine, Beihang University, Beijing, China
[d] HKUST Shenzhen Research Institute, Shenzhen, China

ARTICLE INFO

Keywords:
Multi-directional printing
Volume decomposition
Mechanical enhancement
Support-effective

ABSTRACT

Multi-axis additive manufacturing exploits additional degrees of freedom to enhance printability and flexibility compared to conventional 3D printing. Among various multi-axis additive manufacturing approaches, multi-directional printing decomposes the printing volume into sub-volumes and assigns individual printing directions to each sub-volume. Multi-directional printing enables support-free fabrication of complex and freeform geometry with minimum setup changes, which though requires elaborate process planning and printing trajectory generation. Current process planning approaches for multi-directional printing focus on support-free fabrication but do not consider the mechanical strength in its volume decomposition planning. Therefore, this paper proposes an integrated strength-support volume decomposition optimization method that simultaneously achieves support-free printing and strength enhancement. The proposed method establishes an optimization problem to enhance the mechanical strength and the support-free index, with the partition planes as the optimization variables. The mechanical strength model is established by finite element analysis, capturing the interlayer and intra-layer strength differences in printing. The final optimization problem is solved via a heuristic beam search algorithm, and confirmative simulation results are verified through multi-axis printing and bending tests on representative 3D models (L-shaped beam, Stanford Bunny, etc.).

1. Introduction

Additive manufacturing (AM) is a promising technology that builds volumetric objects through layer-by-layer printing. It has been widely used in the automotive, aerospace, and medical industries due to its manufacturing flexibility and quick prototyping for product customization [1]. Among various layer-wise AM technologies, fused deposition modeling (FDM) and directed energy deposition (DED) are the representative ones that involve synchronized movements of the printing platform and the nozzle. Therefore, their path and process planning, including building orientation setup, slicing, support generation, and path generation for material filling, is crucial to printing accuracy, cost and part strength [2,3].

In layer-wise AM, the fabrication of complex parts with strength retention is one of the most challenging issues due to its layer-by-layer nature and anisotropic printing performance [4]. To improve the mechanical behavior of fabricated parts, it is necessary to understand the relationship between processing parameters and mechanical properties. The mechanical performance of the printed parts, such as tensile strength, compressive strength, Young's modulus, and failure modes, are different along the intra-layer and interlayer printing directions [5–9]. The difference can be easily verified with finite element analysis (FEA) simulation and experiments. The tensile strength of printed parts along the axial direction is proved to be much stronger than along the transverse and out-of-plane directions [8], while the compressive strength is not significantly affected by the build direction [5]. Such mechanical anisotropy arises from the weaker adhesion between adjacent layers, which is caused by the reduced interaction and entanglement of the polymer chains [10]. Another significant characteristic of layer-wise AM is that materials have limited admissible overhang angles and they need support for overhang features. However, support structures increase the printing time, materials cost, and the risk of surface damage during post-processing [11].

Multi-axis AM technique is one promising solution to alleviate the

* Corresponding author.
E-mail address: mektang@ust.hk (K. Tang).

https://doi.org/10.1016/j.addma.2023.103529
Received 2 January 2023; Received in revised form 3 March 2023; Accepted 27 March 2023
Available online 29 March 2023

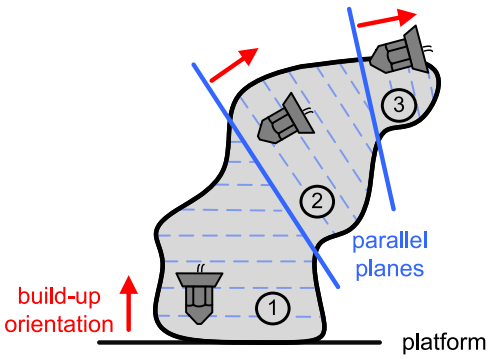

Fig. 1. Schematic diagram of part-based volume decomposition with planar slicing for multi-directional printing.

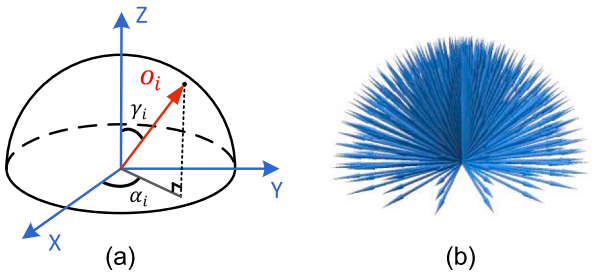

Fig. 2. (a) Definition of $o_i$by a longitude angle α_i and a latitude angle γ_i on hemisphere and (b) their uniformly sampled orientations.

limitations of layer-wise AM. In contrast to the traditional fixed-directional AM, multi-axis AM offers more degrees of freedom (DOFs), enabling translation and variable nozzle orientation of the printing system. On the other hand, the increased flexibility due to additional DOFs requires more general and flexible process and path-planning algorithms. Volume decomposition is typically required to generate the stacking of layers for material deposition. Current volume decomposition methods can be generally classified into layer-based and part-based types. The layer-based methods generate curved layers directly from geometric features of volumetric parts, either by scalar fields [12,13] or convex primitive layers [14–16], where the build orientation changes continuously. However, curved layers induce the local gouging issue for concave layers and the potential intersection between adjacent layers catering for continuous multi-axis printing. Also, consecutive changes of build-up orientation increase the time cost.

The part-based methods, by contrast, divide the specimen into sub-parts and slice them into planar layers for implementing multi-directional printing [4]. As Fig. 1 shows, this multi-directional printing approach intermittently alters the build-up orientation, thus avoiding the local gouging issue in the layer-based methods. The optimized multi-directional process planning aims to enhance mechanical performance/accuracy and reduce support usage and cost [14,15]. A decomposition optimization problem regarding printing quality and structural soundness of fabricated parts was first formulated by Luo et al. [16], wherein the sub-parts are assembled instead of continuously printed. Subsequent research extended the work into multi-directional AM and developed algorithms of volume decomposition optimization for support-effective fabrication through geometric recognition [17–19], exhaustive search [20] or heuristic algorithms [21–24]. The exhaustive search method is computationally robust but may result in suboptimal solutions, while heuristic techniques enable global optimization of decomposition [23], but their effectiveness is limited in some complex geometries [21,22]. Nonetheless, part-based volume decomposition still suffers from weak mechanical strength as it does not extensively optimize the build orientations considering the mechanical strength (unlike the methods in the layer-based volume decomposition work [25–27]). Ulu et al. [18] tried to find the best overall build-up orientation to maximize structural robustness and verified their orientation robustness through experiments. Expanding from single to multiple orientations, Hildebrand et al. [28] developed an orthogonal decomposition approach considering three basis of build-up orientations in terms of printing speed and tensile strength, which is superior to unidirectional printing but insufficiently optimized. Alternatively, Guan et al. [29] achieved better strength retention between adjacent sub-parts by increasing intermolecular penetrating diffusion via gas laser heating.

To sum up, most existing part-based volume decomposition methods have not considered the mechanical strength and support effectiveness simultaneously. To fill this gap, this paper develops a strength-enhanced support-effective volume decomposition (SESEVD) optimization framework (Section 2) to improve the mechanical strength of fabricated parts while at the same time reducing the support usage fulfilling continuous fabrication requirements. This framework utilizes FEA simulation results to evaluate the mechanical behavior of fabricated parts, and the resultant maximal principal stress direction is encouraged to be locally perpendicular to the build orientation via decomposition, while at the same time, for strength enhancement, the decomposition is avoided to be settled at high-stress regions. The support usage is also reduced through build-orientation-dependent overhang face area minimization. A heuristic beam-searching algorithm is developed to determine the optimized decomposition solution within the discrete search space. In Section 3, the computational simulations are conducted on several representative 3D models (L-shape beam, Stanford Bunny, mechanical mounter), and the following bending tests of fabricated models are used to verify the optimization tailoring the mechanical properties and supportless printing. Finally, Section 4 concludes the investigations and the effectiveness of the proposed framework resulting from the computational optimization and experiments.

2. Optimization of SESEVD for multi-directional printing

2.1. Preliminaries

Our volume decomposition and its corresponding process planning comprise the following two main phases: 1) Given an input 3D mesh model $\mathscr{M}$, the decomposition strategy divides the model into a few sub-parts $\mathscr{V}_i$ by a sequence of planes $\mathscr{P}_i$, indicating multiple build orientations; and 2) planar layers and their corresponding continuous printing paths are generated for sub-part printing. The input $\mathscr{M}$ is assumed to be a tetrahedron mesh, while its boundary is a set of triangular faces, regarded as a surface mesh $\mathscr{S}$. Hereafter, a single triangular face e and a single tetrahedral cell ℓ are deemed the elementary units for $\mathscr{S}$ and $\mathscr{M}$, respectively.

The proposed optimization scheme starts with generating a bunch of discrete candidate planes serving as the searching space. We generate candidate planes by sampling a number of orientations in Euclidean space. As shown in Fig. 2(a), the orientation $o_i$is defined by a longitude angle α_i and a latitude angle γ_i, where $\alpha_i \in [0, 360°]$, $\gamma_i \in [0, 90°]$. By controlling the step-increase size of parameters $\Delta\alpha$and$\Delta\gamma$, the candidate build orientation set is uniformly sampled on a hemisphere, as Fig. 2(b) shows, and written as $\mathrm{O} = \{\boldsymbol{o_1}, \boldsymbol{o_2}, \ldots \boldsymbol{o_n}\}$. Given the sampled orientation set O and surface mesh $\mathscr{S}$, for each $\boldsymbol{o_i} \in \mathrm{O}$, its equi-distant parallel planes are induced, and let Π denote the infinite set of all such planes. In the plane set Π, an arbitrary candidate plane π_i is defined by four parameters, written as (a_i, b_i, c_i, d_i), where the vector of (a_i, b_i, c_i) indicates the normal direction $\boldsymbol{o_i}$ of plane and $d_i$is the distance from the plane to the origin. We mathematically define the positive half-space of π_i as $h_i^+ \equiv \{(x, y, z) | \, a_i x + b_i y + c_i z \geq d_i\}$, and the negative half-space as h_i^-. A plane intersecting with the model is used to geometrically identify the decomposition operation. Considering the ith partitioning towards the model by π_i, the model represented by $\mathscr{M}_i(\mathscr{S}_i)$ is separated into two, where the part on the side of $h_i^+$is marked by $\mathscr{M}_i^+(\mathscr{S}_i^+)$ and the one

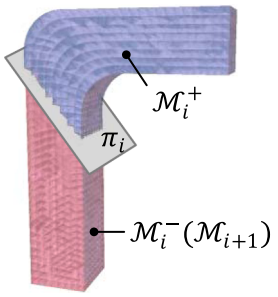

Fig. 3. Part decomposition of $\mathcal{M}$ into its positive part $\mathcal{M}_i^+$ and negative part $\mathcal{M}_i^-$ by plane π_i.

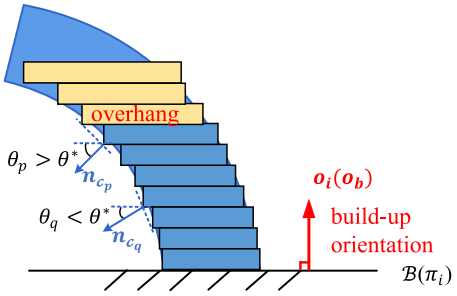

Fig. 4. Overhang condition of the boundary faces c_p and c_q under the direction $o_i(o_b)$ (θ^* denotes the threshold angle).

within h_i^- is marked by $\mathcal{M}_i^-(\mathcal{S}_i^-)$, as Fig. 3 shows. The negative part $\mathcal{M}_i^-$ also decides the $(i+1)$th model $\mathcal{M}_{i+1}$, with $\mathcal{M}_0 = \mathcal{M}$, which is to be partitioned subsequently. Note that, as the tetrahedron mesh $\mathcal{M}$ is assumed to be very fine, to save the computing time, if a tetrahedron cell ℓ intersects π_i, the entire ℓ will be put into h_i^+ if the centroid of ℓ is above π_i, and vice versa.

2.2. Definition of fabrication criteria and objective functions

The SESEVD process planning for multi-directional printing needs to satisfy the collision-free criterion while trying to increase the mechanical strength and reduce the overhang areas. The collision-free criterion is formulated as an optimization constraint, while the support effectiveness and enhanced mechanical strength are formulated as objectives.

Criterion I: collision-free criterion.

Let us set that the initial base platform $\mathcal{B}$ is in the XY plane and the default build orientation $o_b = (0,0,1)$. As build orientation changes in multi-directional printing, collision risk increases between the deposition device and the base platform $\mathcal{B}$. To avoid collision, collision-free criterion between the plane π_i (as a potential building platform for the following sub-part) and the platform $\mathcal{B}$ is given by

$$\pi_i \bigcap \mathcal{B} = \varnothing. \tag{1}$$

Criterion II: support-free criterion.

Fig. 4 illustrates the overhang condition of triangular faces under a build orientation o_b specified by the base platform $\mathcal{B}$, which is equally applied to any plane π_i whose normal direction determines the building direction o_i. The overhang angle threshold is denoted by θ^*, which is generally set to 45°. Let n_{c_p} represents the normal direction of any triangular face c_p on boundary mesh $\mathcal{S}$. For each c_p on $\mathcal{S}$, its overhang condition under a specific building orientation o_i is estimated by the following criterion,

$$n_{c_p} \bullet o_i + \sin(\theta^*) < 0. \tag{2}$$

The faces satisfying this criterion are called overhang faces, otherwise called overhang-free faces. Upon checking the triangular face c_p belonging to $\mathcal{S}_i^+$ (the surface mesh $\mathcal{S}$ above the building plane π_i), the support effectiveness of π_i is denoted by $S(\pi_i)$ and defined by adding up all the overhang faces' areas as follows:

$$S(\pi_i) = \sum_{c_p \in \mathcal{S}^+} h(n_{c_p}, o_i) s(c_p) < \mathrm{h_{max}}, \tag{3}$$

$$h(n_{c_p}, o_i) = \begin{Bmatrix} 1, & \text{overhang} \\ 0, & \text{overhang} - \text{free} \end{Bmatrix}, \tag{4}$$

where $h(n_{c_p}, o_i)$ is a Boolean function that clarifies the overhang condition of c_p, depending on the build orientation o_i and face normal n_{c_p}; and $s(c_p)$represents the face area of c_p. An allowable overhang area threshold $\mathrm{h_{max}}$ is set to guarantee the support effectiveness of π_i.

Objective 1: minimizing the alignment between the build orientation and the stress direction.

The goal of enhanced mechanical performance is achieved by minimizing the maximal principal stress accumulation and the overlap of the partitioning planes with the high-stress regions. Specifically, the maximal principal stress directions are encouraged to align within the deposited layers due to the anisotropic mechanical properties of layer-wise fabricated parts [8,27]. The principal stresses are derived from the second-order Cauchy stress tensor σ associated with a tetrahedral cell ℓ, given by

$$\sigma = \begin{pmatrix} \sigma_{11} & \sigma_{12} & \sigma_{13} \\ \sigma_{21} & \sigma_{22} & \sigma_{23} \\ \sigma_{31} & \sigma_{32} & \sigma_{33} \end{pmatrix}. \tag{5}$$

This symmetric tensor, by eigenvalue decomposition, defines three principal stress vectors σ_1, σ_2, and σ_3, satisfying $|\sigma_1| > |\sigma_2| > |\sigma_3|$. It also defines the scalar von Mises stress σ_v (commonly used to determine the material yielding) given by

$$\sigma_v = \sqrt{\frac{(|\sigma_1| - |\sigma_2|)^2 + (|\sigma_2| - |\sigma_3|)^2 + (|\sigma_3| - |\sigma_1|)^2}{2}}. \tag{6}$$

Tetrahedral cells with high stress σ_v exceeding a specified threshold σ_{th} define the risky region $\mathcal{R}$ (which may be disjointed), where the partitioning plane π_i is discouraged from passing through. To quantitatively evaluate the mechanical performance of the printed part resulting from the decomposition, the objective function $J_1(\pi_i)$ is defined as the superposition of alignment between the build orientation and the maximal principal stress direction over the printing volume, considering the anisotropic mechanical properties of layer-wise fabricated parts. Besides, instead of imposing a strict constraint that prohibits the decomposing plane from intersecting with risky cells, a penalty function q is involved in $J_1(\pi_i)$ to softly constrain the decomposition near risky regions. Consequently, by considering the maximal principal stress σ_1 and the risky region $\mathcal{R}$, a part strength evaluation function optimizing a candidate plane π_i is defined as

$$J_1(\pi_i) = \left(\frac{\sum_{\ell_p \in \mathcal{M}_i^+} |o_i \cdot \sigma_{1,p}|}{N_{\mathcal{M}^+}} + \frac{\sum_{\ell_p \in \mathcal{M}_i^-} |o_b \cdot \sigma_{1,p}|}{N_{\mathcal{M}^-}} \right) q, \tag{7}$$

$$q = \left(1 + \frac{c_N}{N_{\mathcal{M}}}\right)^{n_q}, N_{\mathcal{M}} = N_{\mathcal{M}^+} + N_{\mathcal{M}^-}. \tag{8}$$

In the above formula, $N_{\mathcal{M}^+}$, $N_{\mathcal{M}^-}$, and $N_{\mathcal{M}}$ denote the tetrahedron cell numbers of $\mathcal{M}_i^+$, $\mathcal{M}_i^-$ and $\mathcal{M}$, respectively. The q is acted as a multiplier where c_N is the number of risky tetrahedrons in $\mathcal{R}$ that intersect with π_i, and n_q is the penalization factor trading off the risky region avoidance and the printing direction alignment. Note that the dot product $|o_i \cdot \sigma_{1,p}|$ defines the projection of the maximal principal stress $\sigma_{1,p}$ of a specific tetrahedron cell $\ell_p$onto the corresponding build orientation $o_i(o_b)$, and

their average values in $\mathscr{M}_i^+$ and $\mathscr{M}_i^-$ represent the build orientation's alignment with the maximal principal directions. The over-stress risk $q(q \geq 1)$ is a penalty function to avoid π_i across $\mathscr{R}$: $q = 1$ indicates no risky tetrahedron cells in $\mathscr{R}$ intersect with π_i, while a larger q indicates more overlap between π_i and $\mathscr{R}$, which fosters a higher tendency to avoid decomposing parts around risky cells potentially.

The measurement of J_1 depends on the stress analysis results and is affected by the setup of external loads and boundary conditions. Accordingly, multiple-loading conditions are considered in J_1 assessment and a positive coefficient $\varphi_{1,k}$ is introduced to weight the kth loading condition, with $\sum \varphi_{1,k} = 1$. The formula Eq. (7) is thus further modified as a linear combination, i.e.,

$$J_1(\pi_i) = \varphi_{1,1} J_{1,1}(\pi_i) + \varphi_{1,2} J_{1,2}(\pi_i) + \ldots \varphi_{1,k} J_{1,k}(\pi_i), \tag{9}$$

where $J_{1,k}(\pi_i)$ corresponds to the kth loading scenario with the respective weight $\varphi_{1,k}$.

Objective 2: minimization of the overhang face area.

The design of any partitioning plane is dedicated to reducing or eliminating the support structure usage. To facilitate it, a measurable indicator of support structure usage $J_2(\pi_i)$ is defined by the cumulative area of residual overhang faces among $\mathscr{S}$, expressed by:

$$J_2(\pi_i) = \sum_{\epsilon_p \in \mathscr{S}^+} h(\boldsymbol{n}_{\epsilon_p}, \boldsymbol{o}_i) s(\epsilon_p) + \sum_{\epsilon_p \in \mathscr{S}^-} h(\boldsymbol{n}_{\epsilon_p}, \boldsymbol{o}_\mathbf{b}) s(\epsilon_p) = \sum_{\epsilon_p \in \mathscr{S}^-} h(\boldsymbol{n}_{\epsilon_p}, \boldsymbol{o}_\mathbf{b}) s(\epsilon_p) \tag{10}$$

Similar to Eq. (4), $h(\bullet)$ and $s(\bullet)$represent the overhang condition and face area of any triangular face ϵ_p, respectively. Due to Criterion II restricting plane π_i to be overhang-free, the cumulative overhang face area above π_i (the first term in Eq. (10)) is assured to be zero. Thus, the determination of J_2 only depends on the calculation of $\epsilon_p$belonging to $\mathscr{S}^-$ under the default orientation $\boldsymbol{o}_\mathbf{b}$. Minimizing J_2 reduces the overhang area in the model, contributing to supportless fabrication.

Combining the two prescribed objective functions (Eqs. (7) and (10)) together to simultaneously addresses mechanical strength enhancement and overhang area reduction, a linear combination of Eqs. (7) and (10) is in order, given by

$$J(\pi_i) = \mu_1 \overline{J}_1(\pi_i) + (1 - \mu_1) \overline{J}_2(\pi_i), \tag{11}$$

$$\overline{J}_1(\pi_i) = \tanh\left(\frac{J_1(\pi_i)}{b_1}\right), \tag{12}$$

$$\overline{J}_2(\pi_i) = \tanh\left(\frac{J_2(\pi_i)}{b_2}\right). \tag{13}$$

The coefficient μ_1 and $1 - \mu_1$ in Eq. (11) describe the weights of each objective accounting in the final score $J(\pi_i)$ as a trade-off between the stress and support-free metrics, while $\overline{J}_1(\pi_i)$ and $\overline{J}_2(\pi_i)$ represent rescaled functions of $J_1(\pi_i)$ and $J_2(\pi_i)$. The rescaled functions introduce hyperbolic tangent function $\tanh(\bullet)$ to unify the different magnitude orders of $J_1(\pi_i)$ and $J_2(\pi_i)$, which are both positives in their domains. The $\tanh(\bullet)$function values $\overline{J}_1(\pi_i)$ and $\overline{J}_2(\pi_i)$ are limited to [0,1] in the domain of $[0, +\infty)$ and approaches asymptote at high values of J_1 and J_2, where b_1 and b_2 are two independent constants. As facilitated by Eqs. (11)-(13), the two representative optimization objectives, i.e., the strength enhancement and supports reduction, are now combined into a single minimization problem.

2.3. Schemes of SESEVD optimization

The established SESEVD optimization model is solved via a heuristic beam search algorithm, considering that the objective functions are highly nonlinear and extremely arduous to evaluate. The beam search is based on an iterative enumeration of the feasible solutions implemented by a searching tree. Unlike greedy search techniques, beam search enables the retention of multiple optimum results at each iteration instead of a single optimum. A parameter $\omega \in \mathrm{N}_+$ is used to define the number of best-performed beams in the search. A larger ω expands the search space, leading to greater possibilities of finding a desirable solution though at the cost of increased search time. Bounded by ω, the search algorithm (Algorithm 1) iteratively evaluates candidate planes in a breadth-search first manner in the search space until the stopping conditions are encountered, and the model is progressively partitioned into sub-parts top-down.

The whole optimization scheme consists of a pre-computation procedure and the volume decomposition optimization procedure via beam-search-based optimization. The pre-computation procedure first determines the surface mesh $\mathscr{S}$ and base $\mathscr{B}$, the sampling candidates of orientation set O and plane set Π, as well as the critical stress region $\mathscr{R}$. Besides, the overhang condition is checked for sampled orientation set O. For $\forall \boldsymbol{o_i} \in \mathrm{O}$, a number of overhang faces on surface mesh $\mathscr{S}$ are marked as overhang face set $\mathscr{C}$. When judging the support effectiveness of plane π_i whose normal direction is $\boldsymbol{o_i}$, it only needs to evaluate the support-free condition for $\epsilon \in \mathscr{C}$ instead of $\epsilon \in \mathscr{S}$.

In the main procedure, i.e., the volume decomposition optimization, the search process starts from the root node $\mathscr{T}_{0,0} = \{\mathscr{M}, \mathscr{P}_{0,0}\}$, which stores the unprocessed model $\mathscr{M}$ and an empty plane list $\mathscr{P}_{0,0}$for decomposition. The search space is defined by Π, where candidate planes with the same $\boldsymbol{o_i}$ are stored in $\Pi_i \in \Pi$, which are ordered based on the coordinates resulting from the model-plane intersection. At each generic iteration t, the search traverses the orientation set $\Pi_i \in \Pi$ sequentially. During orderly searching through Π_i, the plane $\pi_{i,j} \in \Pi_i$ is first examined by the fabrication criteria. The plane $\pi_{i,j}$ violating the collision-free criterion (Criterion I) is abandoned and the search jumps to $\pi_{i,j+1} \in \Pi_i$, while if the support-free criterion (Criterion II) is not met, the search skips to Π_{i+1}. The qualified planes that satisfy both criteria, defining the set $\mathscr{D}$ of candidate descendants, are then evaluated following Eqs. (7)-(13), and the evaluation scores $J(\pi_{i,j})$ are obtained accordingly. Afterwards, the set $\mathscr{D}$ is sorted according to the evaluation scores to select its descendant node for the construction of the next level $\mathscr{T}_{t+1,k}$, where t denotes the current iteration number and k denotes the reserved number bounded by ω. By minimizing the proposed objectives, the ω current best-performed planes $\pi^*_{t+1,k} (k = 1, 2, \ldots, \omega)$ are selected according to the order and stored in the plane list $\mathscr{P}_{t+1,k}$. The mesh $\mathscr{M}$ is decomposed by plane $\pi^*_{t+1,k}$ to get $\mathscr{M}_k^-$ for the subsequent iterations. The resultant component $\mathscr{M}_k^-$ and the corresponding plane list $\mathscr{P}_{t+1,k}$ are thus stored in the tree node as $\mathscr{T}_{t+1,k} = \{\mathscr{M}_k^-, \mathscr{P}_{t+1,k}\}$. The corresponding update for surface mesh $\mathscr{S}$, candidate planes Π, and the overhang face set $\mathscr{C}$ are implemented as well. Such iterations are repeated until the stopping criteria are reached. The stopping criteria for the beam search include two possibilities. The first one is that the anticipated ω beam nodes are filled with qualified decomposition solutions, where a node $\mathscr{T}_{t,k} = \{\mathscr{M}_k^-, \mathscr{P}_{t,k}\}$ is regarded as a beam node when $\mathscr{M}_k^-$ satisfies the support-free conditions within the allowable threshold. Another stopping situation is that a prescribed maximum number of partitioning operations, denoted by n_c, is reached. As a result of the search operation, a specific number of decomposition solutions $\mathscr{G}_{b,k} (k \leq \omega)$ are obtained.

A single group of decomposition solution $\mathscr{P}_k \in \mathscr{G}_{b,k}$ consists of a sequence of feasible partition planes $\pi_1{}^*, \pi_2{}^* \ldots \pi_N{}^*$. The N planes decompose the model into $N+1$ sub-parts, and the resultant sub-parts satisfy the following relation:

$$\mathscr{M} = \mathscr{M}_1^+ \cup \mathscr{M}_2^+ \ldots \cup \mathscr{M}_N^+ \cup \mathscr{M}_N^-. \tag{14}$$

The overall score of $\mathscr{P}_k$ is calculated by summing up the evaluation values of all the involved planes, given by

$$S(\mathscr{P}_k) = \sum_{\pi_k \in \mathscr{P}_k} J(\pi_k{}^*). k \in [1, N]. \tag{15}$$

By minimizing the $S(\mathscr{P}_k)$ among all feasible solutions in $\mathscr{G}_{b,k}$, the

solution $\mathscr{P}^*$ with a minimal score $S(\mathscr{P}^*)$ is selected as the optimal decomposition strategy. The pseudo-code for the prescribed SESEVD optimization is outlined in Algorithm 1.

Algorithm 1. The SESEVD optimization.

Input: a tetrahedra mesh $\mathcal{M}$,
stress $\sigma_v, \boldsymbol{\sigma}_1$ for $\forall t \in \mathcal{M}$,
maximal number of partitions and solutions n_c, ω,
sampling coefficient $\Delta\alpha, \Delta\gamma$.
Output: the volume decomposition solution $\mathcal{P}^*$

/* Procedure: PRE_COMPUTATION */
$\mathcal{S}, \mathcal{B}$ = GetBoundary ($\mathcal{M}, \boldsymbol{o}_b$)
O, Π = GetCandidates($\Delta\alpha, \Delta\gamma$)
$\mathcal{R}$ = SetCriticalRegion ($\mathcal{M}, \sigma_v, \boldsymbol{\sigma}_1$)
C = ComputeOverhangFaceNum($\mathcal{S}, O$)
/* Procedure: OPT_DECOMPOSITION*/
  $t = 0$
  Assign $\{\mathcal{M}, \mathcal{P}_{t,0}\}$ to tree node $\mathcal{T}_{t,0}$
  $\mathcal{G}_{b,k} = \emptyset$
  while true
    $\mathcal{D} = \emptyset$
    for all $\Pi_i \in \Pi$ **do**
      for all $\pi_{i,j} \in \Pi_i$ **do**
        if $S(\pi_{i,j}) < oh^*$ /* Criterion II, Eq. (3) */
          if $\pi_{i,j} \cap \mathcal{B} = \emptyset$
            continue /* Criterion I, Eq. (1) */
          else
            $J(\pi_{i,j})$ = PlaneEvaluation($\pi_{i,j}, \sigma_v, \boldsymbol{\sigma}_1, \mathcal{S}, \mathcal{B}, \mathcal{R}, C$) /* Eq. (7)-(13) */
        else break
        Add $(\pi_{i,j}, J(\pi_{i,j}))$ to candidate descendants $\mathcal{D}$
    $\pi^*_{t+1,k} = \arg\min_{\pi_{i,j}} \mathcal{D}(J(\pi_{i,j}))$
    for each $\pi^*_{t+1,k}$
      $\{\mathcal{M}^+_k, \mathcal{M}^-_k\}$ = MeshDecomposition($\mathcal{M}, \pi^*_{t+1,k}$)
      Assign $\{\mathcal{M}^-_k, \mathcal{P}_{t+1,k}\}$ to the tree node $\mathcal{T}_{t+1,k}$
      if $\mathcal{M}^-_k$ is support-free
        Add $\mathcal{T}_{t+1,k}$ to $\mathcal{G}_{b,k}$
      $\mathcal{M} = \mathcal{M}^-_k, \mathcal{S} = \mathcal{S}^-_k$
    if size($\mathcal{G}_{b,k}$) ≥ ω OR $t \geq n_c$ **then**
      $\mathcal{P}^* = \arg\min \mathcal{G}_{b,k}\left(S(\mathcal{P}_{b,k})\right)$ /* Eq. (15)*/
    return $\mathcal{P}^*$
  $t = t + 1$

The printing sequence design between different sub-parts is crucial in process planning, as it may cause collisions between the deposition device and the fabricated parts. In this study, the decomposition process naturally defines the printing sequence as the solution $\mathscr{P}^*$ provides a sequence of planes in a top-down order for partitioning $\mathscr{M}$, which is opposite to the printing sequence between the sub-parts (bottom-up). In addition, the mesh-decomposition process after each iteration ensures no fabricated parts above the partition plane, thereby preventing potential collisions. The printing sequence is not explicitly designed for multiple sub-parts in $\mathscr{M}^+$ from any single partitioning so that the deposition sequences are switched between sub-parts in each layer.

3. Simulation and experiment results

The proposed SESEVD optimization method was verified through computational simulation on three representative models: an L-shaped beam, a mechanical mounter, and a Stanford bunny. The tested models were created in Solidworks and meshed into tetrahedral elements.

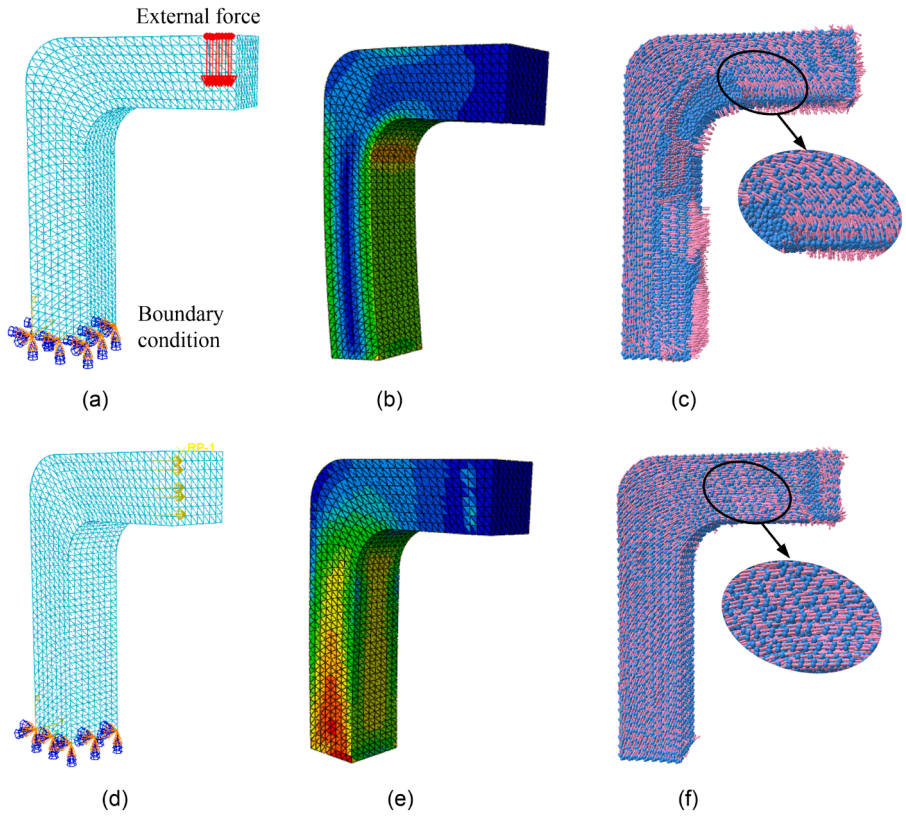

Fig. 5. (a), (d) FEA simulation setups, (b), (e) resultant von Mises stress contours, and (c), (f) maximal principal stress flows under two loading scenarios on the L-shaped beam.

Before applying the optimization procedure, the stress analysis was first carried out on the tetrahedral models in C3D10 element type by the commonly used FEA commercial software ABAQUS. Multiple loading scenarios were studied via stress analysis using PLA material under the isotropic material assumption. The adopted PLA material parameters are Young's modulus of 2.3 GPa, Poisson's ratio of 0.37, and density of $1.25 \mathrm{g/cm}^2$.

The established optimization procedure in Algorithm 1 was

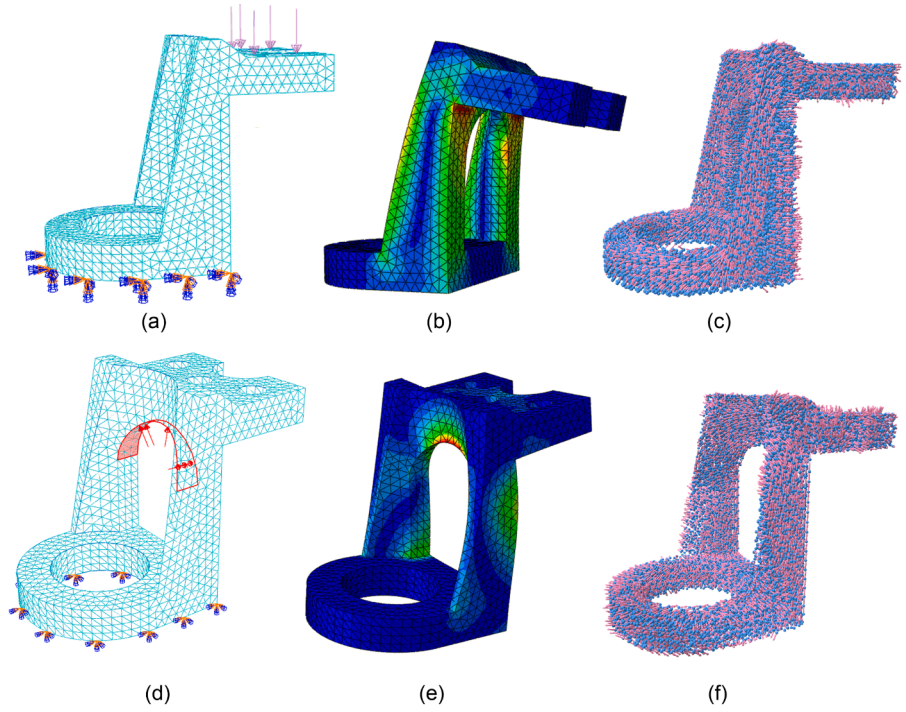

Fig. 6. (a), (d) FEA simulation setups, (b), (e) resultant von Mises stress contours, and (c), (f) maximal principal stress flows under two loading scenarios on the mechanical mounter.

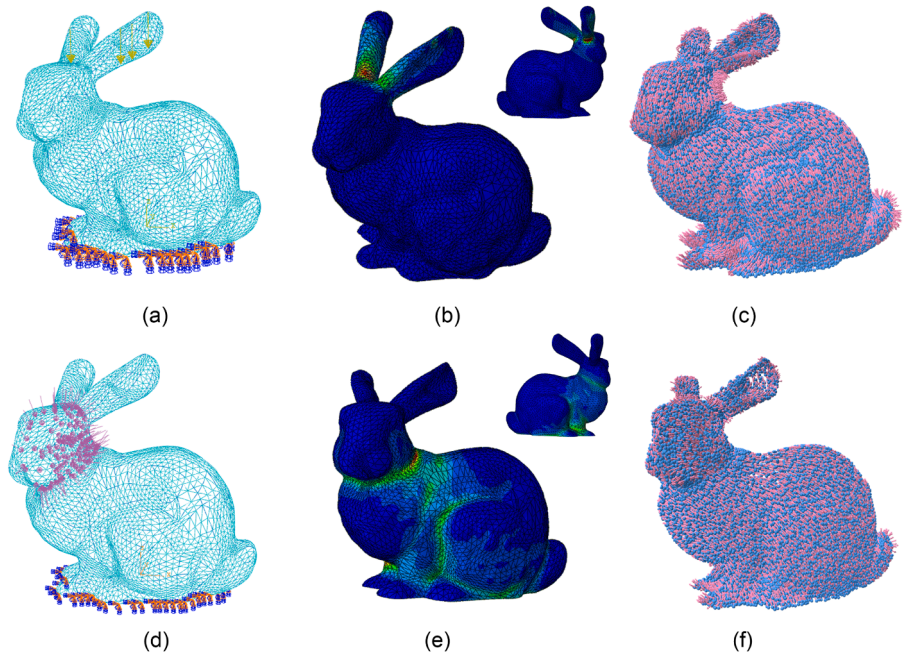

Fig. 7. (a), (d) FEA simulation setups, (b), (e) resultant von Mises stress contours, and (c), (f) maximal principal stress flows under two loading scenarios on the Stanford bunny.

implemented in C+ +, while $\omega = 4$ bounds the heuristic beam search as a balance of optimization performance and computational efficiency. In the following case studies, the candidate orientations and planes were sampled by parameters $\Delta\alpha = 10^\circ, \Delta\gamma = 5^\circ$; the maximum allowable partition number $n_c = 6$ was used to terminate the search process. The SESEVD optimization procedure was first simulated on the L-shaped beam subject to both single-loading and multiple-loading conditions. The objective function Eq. (11) defines the coefficient μ_1 addressing the importance of stress-metric in evaluation, indicating that the selection of μ_1 influences the optimization solutions. Accordingly, several SESEVD optimizations were performed with μ_1 changing from 0.1 to 0.9 with a step of 0.1. Besides, a mechanical mounter (with non-zero genus geometry) and a Stanford bunny (with complex geometrical features) were simulated under single-loading conditions to demonstrate our algorithm's robustness. Finally, bending tests were further conducted on several fabricated L-shaped beam specimens to investigate the effects of the strength weight μ_1 on optimized SESEVD solutions and to identify part strength improvements through optimization.

3.1. Simulation results

The FEA simulations on three test models (L-shaped beam, mechanical mounter and Stanford bunny) are presented in Fig. 5, Fig. 6 and Fig. 7, respectively. For each model, two individually applied loads are shown in (a) and (d) of their corresponding diagram, where the arrows indicate the loading directions and cones denote the fixed boundary conditions. The Cauchy tensors were obtained through simulation, and the resultant von Mises stress contours under the corresponding loading conditions were visualized in (b) and (e) on the tested models. Derived by the Cauchy tensor, the maximal principal stress $\boldsymbol{\sigma}_I$ for each tetrahedral cell $\mathcal{e}$ was calculated following Section 2.2. Besides, the diagrams gave a macroscopical view of the maximal principal stress flows among $\mathcal{M}$ in (c) and (f), where the blue dots with pink arrows indicate the unit directions of $\boldsymbol{\sigma}_I$ on the centroid of $\mathcal{e}$. As a result, the maximal principal stress and von Mises stress resulting from the FEA simulation were utilized in Eq. (7) for J_1 evaluation, and $n_q = 3$ was adopted in Eq. (8) to define the penalization factor.

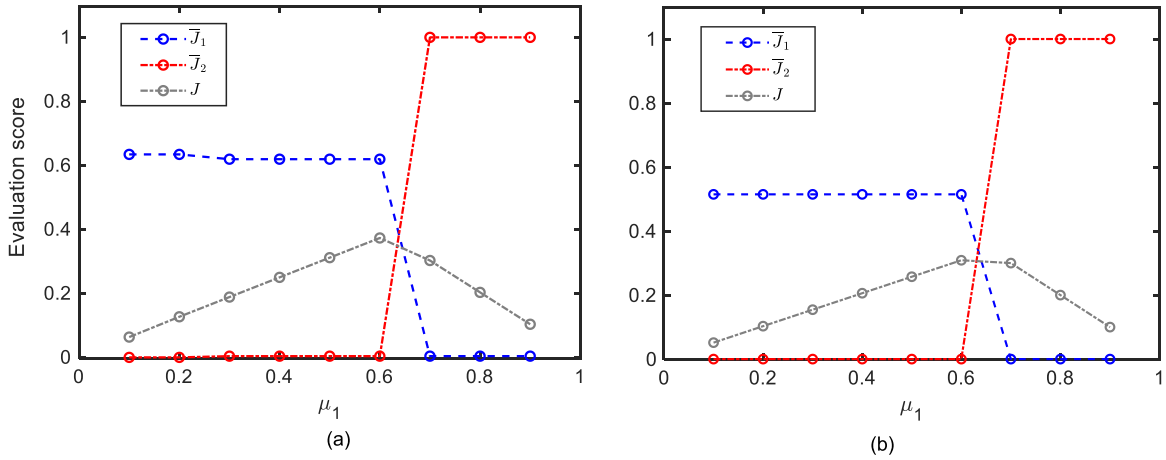

Fig. 8. Evaluation score $(\overline{J}_1, \overline{J}_2, J)$ of decomposition solution with the variation of strength weight μ_1 under (a) single-loading conditions and (b) multiple-loading conditions.

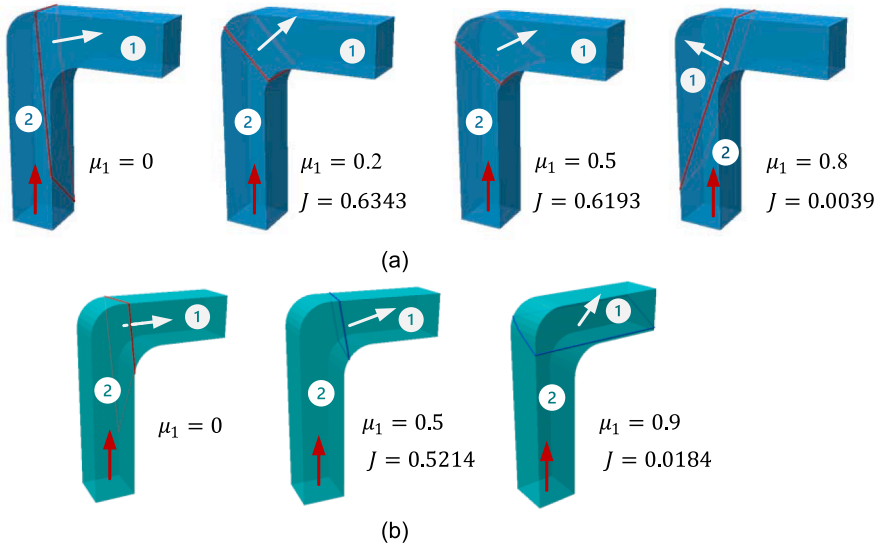

Fig. 9. Optimized SESEVD solution for L-shaped beam with specific μ_1 under (a) single-loading and (b) multiple-loading conditions.

Through the established Algorithm 1, computational simulations were first adopted on the L-shaped beam. The evaluation scores $\bar{J}_1$, $\bar{J}_2$ and J of the optimized solutions with different u_1's were shown in Fig. 8, where (a) and (b) showed the trend under the single-loading condition and multiple-loading condition, respectively, corresponding to the load setups in Fig. 5. Observed from the diagram, increasing of μ_1 from 0.1 to 0.9 decreases $\bar{J}_1$ and increases $\bar{J}_2$ on the whole, while the overall score $J = \mu_1\bar{J}_1 + (1-\mu_1)\bar{J}_2$ rises first and then descends. The reason is that in the small μ_1 situation, the dominant factor in optimization is the support-free metric so that the influence of $\bar{J}_1$ on J is much weaker than $\bar{J}_2$. Therefore, it is concluded that μ_1 is an effective tuning variable to balance between the strength and the support effectiveness metric.

The optimum SESEVD solutions obtained from Fig. 8 under specific μ_1 were visualized in Fig. 9 and all of them led to a single partition plane. Fig. 9(a) shows the solutions under the single-loading condition, with arrows indicating the build orientation and serial numbers marking the sub-parts sequence top-down. As the results indicated, a single partition plane defined by the outline is obtained through SESEVD among different strength weight μ_1. Among solutions of $\mu_1 = 0, 0.2, 0.5, 0.8$, the limiting case of $\mu_1 = 0$ was obtained by merely optimizing the support-free metric ($\bar{J}_2$) to compare with the strength-enhanced cases ($\mu_1 > 0$). It is noted that, for the case of $\mu_1 = 0$, when identical scores obtained from $\bar{J}_2 = 0$ result in multiple feasible solutions, the one with the highest $\bar{J}_1$ value is selected. Similarly, the optimal solutions subject to the multiple-loading condition were given in Fig. 9(b) for $\mu_1 = 0, 0.5, 0.9$, while a larger difference between (a) and (b) were found in the cases of $\mu_1 > 0.5$ due to the multiple-loading scenarios involved. In this case, two loading scenarios were implemented with assigned $\varphi_{1,1} = \varphi_{1,2} = 0.5$ in Eq. (9), indicating the two loading conditions are of equal importance. Moreover, when considering the single-loading condition with $\mu_1 = 0.8$ and the multiple-loading condition with $\mu_1 = 0.9$, the optimization results in solutions with large overhang areas. It is indicated that selecting high values of μ_1 prioritizes the optimization of the strength metric while simultaneously weakening the support-free metric. To provide guidance on the selection of μ_1, an area threshold A^* is introduced as the maximum tolerable overhang face area for comparison with the J_2 score. In cases where the decomposition solution results in excessive overhang area left ($J_2 > A^*$), the value of μ_1 can be decreased. It is important to note that the choice of μ_1 is dependent on the specific requirements of the parts being fabricated. In cases where the part has a higher demand for strength performance, higher μ_1 is more appropriate. Based on the case analysis of μ_1, a weight of 0.5 is adopted in this paper for adopting a general optimization procedure on test models for the lateral physical experiment, implying the equal importance of mechanical attributes and support-free metric in achieving desired volume decomposition.

Consequently, the SESEVD simulations with $\mu_1 = 0.5$ were performed on a total of three models, and the computational statics are concluded in Table 1. Fig. 10 showcases the optimized solutions for the L-shaped beam, Stanford bunny, and mechanical mounter models, considering both single-loading and multiple-loading conditions. Specifically, (a)-(c) depict the models partitioned into 2, 5, and 2 sub-parts under a single-loading condition, while (d)-(f) display the solutions partitioned into 2, 6, and 2 sub-parts, respectively, under a multiple-loading condition. The optimization results reveal that the L-shaped beam and Bunny yield distinct decomposition solutions, whereas the mechanical mounter exhibits similar solutions for both loading conditions. The sub-parts, identified by different colors, were sliced into planar layers within the user-defined thickness, whereas the serial number defines the search sequence, which is reversed from the printing sequence. One thing to mention is that, for the Bunny case, the overhang faces connected to the platform $\mathscr{B}$ were waved from optimization since the default orientation $\boldsymbol{o}_\mathbf{b}$ was regarded as fixed in this study; therefore, it cannot be support-free but only within the allowable threshold without changing $\boldsymbol{o}_\mathbf{b}$.

Table 1
Computational statistics.

Model	Cell numbers	Sampling size	Loading condition numbers	Sub-part numbers	Computing time
L-shaped beam	23006	13196 planes (667 direction)	1 2	2 2	365 s 425 s
Mechanical mounter	16904	16436 planes (667 direction)	1 2	2 2	288 s 276 s
Bunny	54264	20990 planes (667 direction)	1 2	5 6	2615 s 3102 s

3.2. Printing experiment results

The test models were physically fabricated using multi-directional

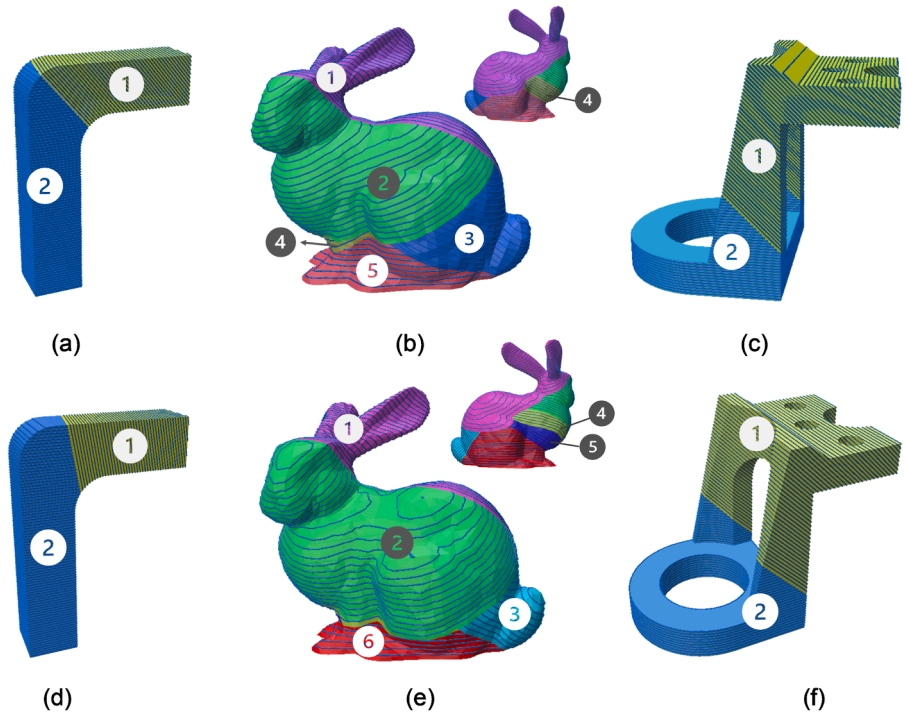

Fig. 10. Optimized SESEVD solutions with strength weight $\mu_1 = 0.5$ for (a) an L-shaped beam, (b) the Stanford bunny, and (c) the mechanical mounter under single-loading condition and multiple-loading condition.

Table 2
Parameters for iso-planar path generation.

Parameter	Raster angle (°)	Layer thickness (mm)	Side-step width (mm)	Nozzle diameter (mm)	Material diameter (mm)
Value	90°	0.4	1	0.4	1.75

printing based on the computational solutions to validate the proposed methodology further. Printing paths were generated using the classical iso-planar approach on the MATLAB platform, followed by decomposition and layer slicing. For the printing pattern on any layer, we adopted the contour-zigzag filling type, where a few parallel contour paths are produced to follow the layer boundary and zigzag paths (i.e., iso-planar paths) are then generated to fill the interior of the layer. Table 2 lists the processing parameters used in path generation, and the details of the iso-planar approach were provided in our previous study [30].

A home-built 6-DOF robotic-arm-based multi-axis printer was used to conduct multi-directional printing using the FDM technique, where the printing paths were received as G-codes. In Fig. 11, (a) displays the printing system, where the end-effector of the robotic arm serves as the base platform to provide 5DOFs in motion, and the nozzle-integrated extrusion system deposits the heated material to fabricate the objects. For effective deposition, the building platform temperature was kept at 60 °C, and the filament was heated to 200 °C during fabrication. Three test models were fabricated based on the simulation outcomes, and their printed counterparts are shown in Fig. 11 (b), (c), and (d) correspondingly. Catering to supportless printing, the L-shaped beam with $\mu_1 = 0, 0.2, 0.5$, the mechanical mounter with $\mu_1 = 0, 0.5$ and the Bunny with $\mu_1 = 0.5$ were chosen for multi-directional printing. For illustrative purposes, Fig. 12 depicts the printing sequence of the Stanford Bunny among multiple parts during the manufacturing process, where each sub-part is distinguished by a unique color to indicate its specific build-up orientation. The sub-parts were printed in a specific order, beginning with the base platform and proceeding with the remaining components.

The bending tests were conducted on fabricated L-shaped beams and the mechanical mounter to measure the ultimate failure forces. As shown in Fig. 13, the bending test was conducted on a universal tensile machine (UTM), Sintech 10/D from MTS, where the specimen was held in place by a fixture placed beneath the load cell. The setups of bending tests on specimens (external loading and fixed boundary) were consistent with the computational simulations demonstrated in Figs. 5(a) and 6(a), respectively, for both the L-shaped beam and the mechanical mounter. Two groups of specimens were tested for each model to account for variability in mechanical testing. During the test, the load cell continuously applied increasing forces on the specimen at a 5 mm/min displacement rate until the specimen broke.

The experimental data with the corresponding decomposition results for L-shaped beams are reported in the diagram of Fig. 14, where two groups of experiments were labeled as #1 and #2. From the extension-loading curve, it was observed that the printed PLA specimens were linearly elastic and relatively brittle. The maximum load that the L-shaped specimens can bear increases with the rise of strength weight μ_1 as a general trend. Table 3 summarizes the L-shaped specimen's fracture characteristics and failure statistics under bending forces with different weights. As the specimen photos in Table 3 indicate, the broken specimens showed brittle bending behavior with sudden failure. For the first group (#1), the ultimate failure forces for the three cases were measured as 660.0 N, 904.1 N and 1136.99 N, respectively. Compared with the control group ($\mu_1 = 0$), the optimized groups ($\mu_1 = 0.2$, $\mu_1 = 0.5$) demonstrated significant improvements in force bearing capacity, with increases of 37.0% and 72.3%, respectively. Similar trends were

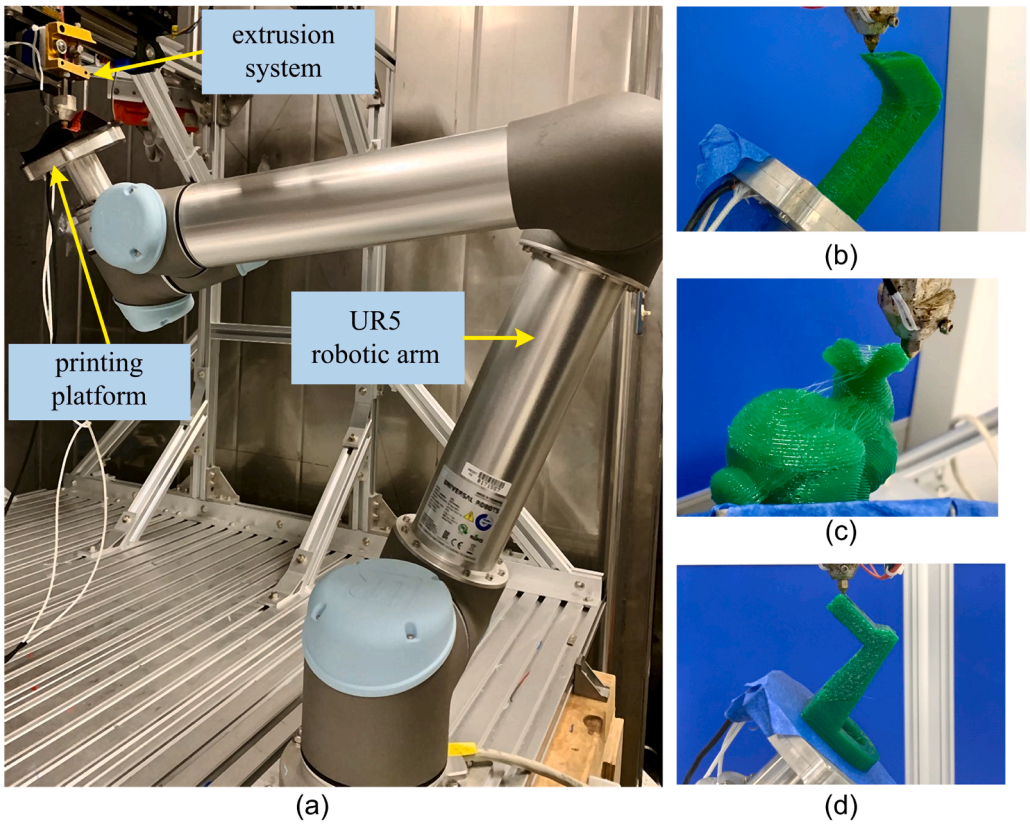

Fig. 11. Physical printing tests by (a) the home-built robotic arm-based multi-axis printing system, and the printed (b) L-shaped beam, (c) Stanford bunny and (d) mechanical mounter.

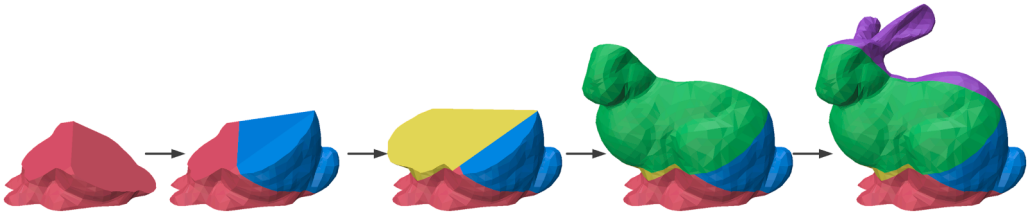

Fig. 12. The support-free printing sequence for Stanford bunny from the SESEVD solution (5 subparts).

investigated in the second group (#2), where the optimized group showed improvements of 63.1% and 143.6%. It also can be seen that the control group without SESEVD optimization (i.e., without maximal principal stress intra-layer alignment and without decomposition avoidance in the critical region) exhibits a higher failure probability at the partition surface. Accordingly, the SESEVD optimization on mechanical properties of layer-wise fabricated parts was thus verified, and it was found that the degree of influence on strength enhancement increased with μ_1. The reason is that, as previously explained in Section 3.1, the solution for $\mu_1 = 0$ only meets support-free metric while another two cases ($\mu_1 > 0$) also considered strength metric by the principal-stress-dependent objective function. In the weighted objective functions (Eq. (11)), the more considerable value of μ_1 implies a greater degree of strength in optimization, thus leading to the fabricated specimens of $\mu_1 = 0.2$.

The bending tests were also adopted on the mechanical mounter, and the resulting experimental data on two groups were presented in Fig. 15 where the group of $\mu_1 = 0.5$ and $\mu_1 = 0$ represent the optimized group and the control group, respectively. Table 4 presents a graphical illustration with test results of the fractured mechanical mounter specimen. To assess the effectiveness of optimization, the bending test results on the optimized group and the control group were compared in Table 4. The findings show an increase of approximately 140% in ultimate failure force, indicating that the optimized group exhibited much better fracture resistance than the control group. Overall, the comparison between the optimized and control groups on the mechanical mounter further

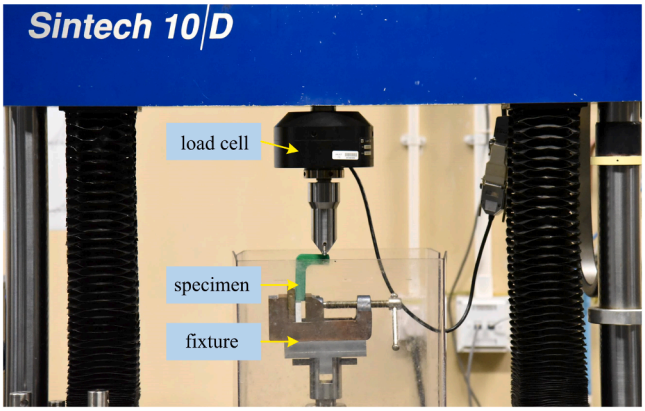

Fig. 13. Bending test setup with UTM - Sintech 10/D from MTS.

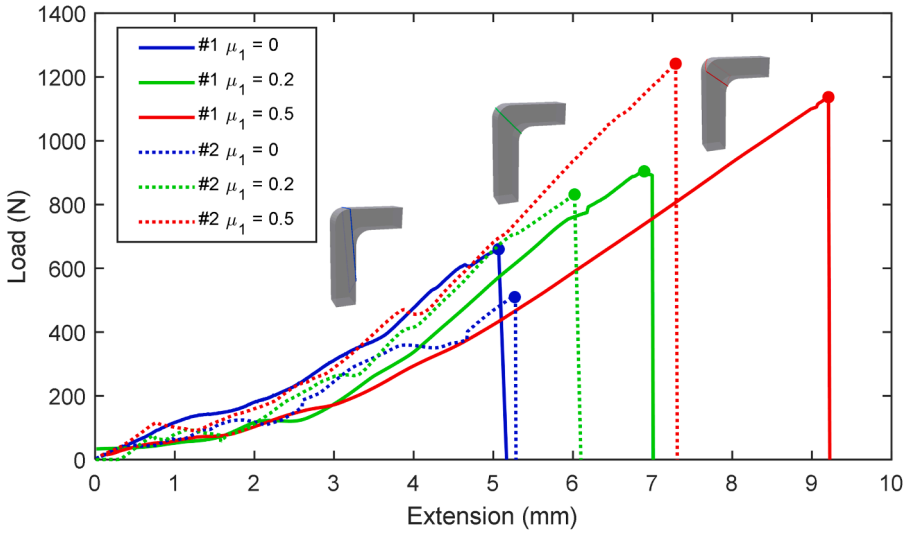

Fig. 14. Experimental comparison of bending tests with different strength weight μ_1 on the L-shaped beam.

evaluates the effectiveness of SESEVD optimization in improving the mechanical properties of the specimens.

The fabrication for the Stanford bunny model was designed to perform fixed-directional printing and multi-directional printing experiments on the same printing system, so to demonstrate the desired improvements in support structure usage. As the Bunny model has distinct overhang features, supporting structures are indispensable when performing fixed-directional printing. Therefore, the paths (including the support structure) for fixed-directional printing were generated using a standard 3D printing software, Ultimaker Cura, with 80% infill support structures in columnar type. By contrast, the bunny part optimized by the proposed SESEVD solution was partitioned into five sub-parts to perform multi-directional printing, as presented in Fig. 10(b). The printed parts by supportless and support-dependent fabrication are shown in Fig. 15, and the experimental data (printing time and material costs) are summarized in Table 5. It is seen that the bunny parts fabricated by the fixed-directional printing consume 11.8% more material and is 10.2% slower than that by the multi-directional printing planned by the proposed SESEVD optimization. The reason is obvious – support structures consume more deposition material deposition, thus causing longer printing time. Besides, fixed-directional printing requires frequent switching between the part itself and the supporting structure, as opposed to the limited number of rotations between sub-parts required by the decomposition-based approach, thus prolonging the printing time. Moreover, as support structures must be eradicated after the part is printed, extra processing time and cost will be required, in addition to the degraded surface quality on the part boundary interfacing the support structures. (Fig. 16)

4. Conclusions

We have presented an optimization framework for integrated process planning of multi-directional layer-wise additive manufacturing (AM). In addition to the support-free metric, strength enhancement is also addressed in the proposed framework by utilizing the anisotropic mechanical properties of materials considering both the intra-layer and inter-layer. The minimization of the proposed measurable objectives is solved by a heuristic beam search algorithm cooperating with continuous fabrication requirements. The computational simulations of the proposed framework are performed on three representative models, followed by real physical FDM multi-axis printing for validation. Based on the experimental results, the effects of the stress weight μ_1, which is the crux of the optimization model for balancing between support effectiveness and strength enhancement, are positively confirmed.

Table 3
Mechanical property of L-shaped beam under bending test with different solutions.

Strength weight μ_1	0		0.2		0.5	
Broken specimens under bending test (single group)	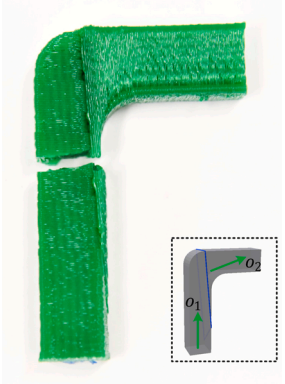		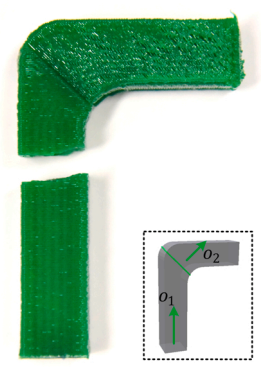		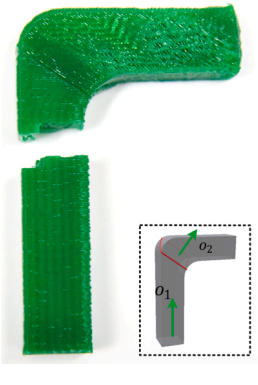	
Group number	#1	#2	#1	#2	#1	#2
Ultimate failure force (N)	660.0	509.7	904.12	831.52	1136.9	1241.8
Improvement	-	-	+ 37.0%	+ 63.1%	+ 72.3%	+ 143.6%

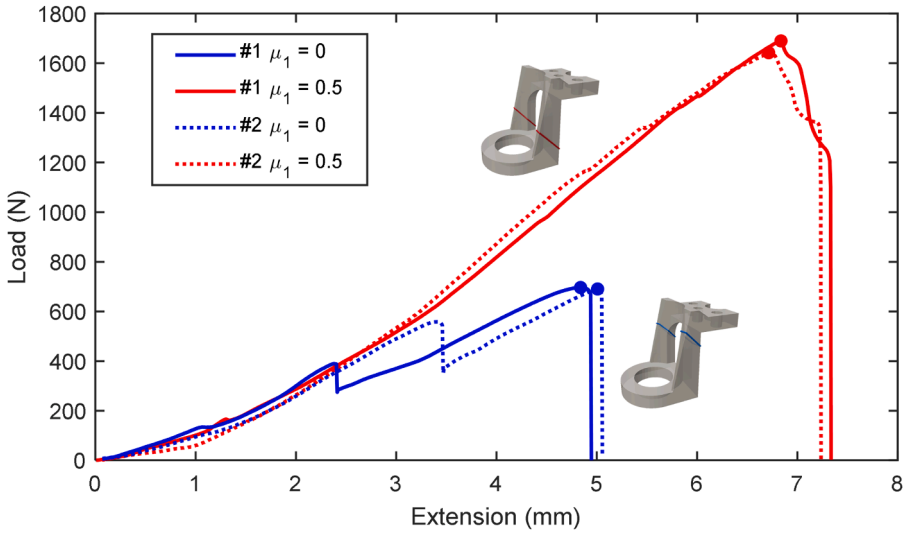

Fig. 15. Comparison of bending test results between the SESEVD optimized and non-optimized group on the mechanical mounter.

Table 4
Mechanical property of the mechanical mounter under bending test with different solutions.

Strength weight μ_1	0		0.5	
Broken specimens under bending test (single group)	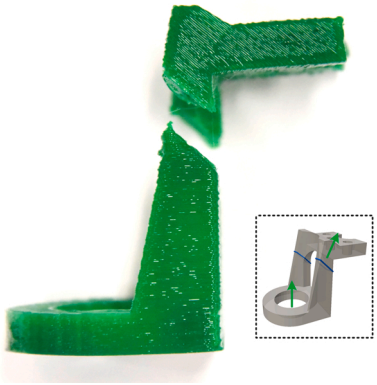		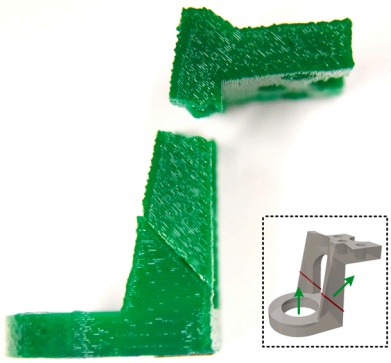	
Group number	#1	#2	#1	#2
Ultimate failure force (N)	696.5	690.5	1689.8	1642.3
Improvement	-	-	+ 142.6%	+ 137.8%

Table 5
Comparison of printing time and material usage.

Fabricated part	Part number	Material usage (mm)		Printing time (s)	
Bunny (fixed-directional)	1	19,249	-	8429.2	-
Bunny (multi-directional)	5	17,219	↓ 11.8%	7649.1	↓ 10.2%

Finally, bending tests are conducted on the fabricated parts, and the results have verified that the proposed optimization framework can increase the strength of fabricated parts while enabling supportless fabrication.

The results presented here are limited to multi-directional printing, and only the FDM type of homogeneous and single deposition material is considered currently. Regarding future research, barring local gouging, printing layers do not need to be planar, or at least though planar but not necessarily parallel. Besides, composite AM has already shown a huge promising potential due to its superior mechanical properties, such as continuous fiber AM, which will be our next focus.

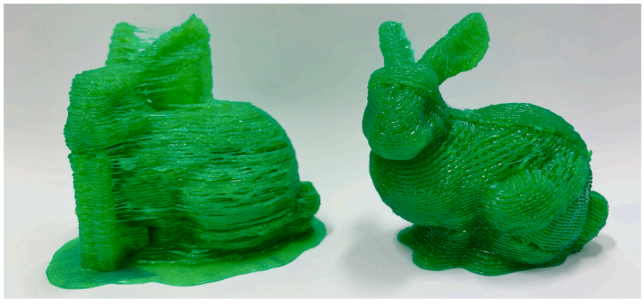

Fig. 16. The fabricated specimens using a fixed build orientation with supports (left) and the optimized decomposition results with multiple printing orientations without supports (right).

CRediT authorship contribution statement

Molong Duan: Supervision, Writing – review & editing. **Kai Tang:** Writing – review & editing, Supervision.

Declaration of Competing Interest

The authors declare that they have no known competing financial interests or personal relationships that could have appeared to influence the work reported in this paper.

Data availability

No data was used for the research described in the article.

Acknowledgements

This work is supported in part by (i) Foshan HKUST Projects (Project ID: FSUST20-SRI09E); and (2) the Project of Hetao Shenzhen-Hong Kong Science and Technology Innovation Cooperation Zone (Project ID: HZQB-KCZYB-2020083).

References

[1] O.A. Mohamed, S.H. Masood, J.L. Bhowmik, "Optimization of fused deposition modeling process parameters: a review of current research and future prospects,", Adv. Manuf. vol. 3 (1) (2015) 42–53, https://doi.org/10.1007/s40436-014-0097-7.

[2] N. Ahsan, B. Khoda, "AM optimization framework for part and process attributes through geometric analysis,", Addit. Manuf. vol. 11 (2016) 85–96, https://doi.org/10.1016/J.ADDMA.2016.05.013.

[3] A.K. Sood, R.K. Ohdar, S.S. Mahapatra, "Improving dimensional accuracy of Fused Deposition Modelling processed part using grey Taguchi method,", Mater. Des. vol. 30 (10) (2009) 4243–4252, https://doi.org/10.1016/j.matdes.2009.04.030.

[4] P.M. Bhatt, R.K. Malhan, A. v Shembekar, Y.J. Yoon, S.K. Gupta, "Expanding capabilities of additive manufacturing through use of robotics technologies: A survey,", no. November 2019, Addit. Manuf. vol. 31 (2020), 100933, https://doi.org/10.1016/j.addma.2019.100933.

[5] S.H. Ahn, M. Montero, D. Odell, S. Roundy, P.K. Wright, "Anisotropic material properties of fused deposition modeling ABS,", Rapid Prototyp. J. vol. 8 (4) (2002) 248–257, https://doi.org/10.1108/13552540210441166.

[6] T. Yao, J. Ye, Z. Deng, K. Zhang, Y. Ma, H. Ouyang, "Tensile failure strength and separation angle of FDM 3D printing PLA material: Experimental and theoretical analyses,", Compos B Eng. vol. 188 (2020), 107894 https://doi.org/10.1016/J.COMPOSITESB.2020.107894.

[7] Y. Zhao, Y. Chen, Y. Zhou, "Novel mechanical models of tensile strength and elastic property of FDM AM PLA materials: Experimental and theoretical analyses,", Mater. Des. vol. 181 (2019), 108089 https://doi.org/10.1016/J.MATDES.2019.108089.

[8] Y. Song, Y. Li, W. Song, K. Yee, K.Y. Lee, V.L. Tagarielli, "Measurements of the mechanical response of unidirectional 3D-printed PLA,", Mater. Des. vol. 123 (2017) 154–164, https://doi.org/10.1016/J.MATDES.2017.03.051.

[9] C.S. Lee, S.G. Kim, H.J. Kim, S.H. Ahn, "Measurement of anisotropic compressive strength of rapid prototyping parts,", J. Mater. Process Technol. vol. 187–188 (2007) 627–630, https://doi.org/10.1016/J.JMATPROTEC.2006.11.095.

[10] Q. Ding, X. Li, D. Zhang, G. Zhao, Z. Sun, "Anisotropy of poly(lactic acid)/carbon fiber composites prepared by fused deposition modeling,", J. Appl. Polym. Sci. vol. 137 (23) (2020) 48786, https://doi.org/10.1002/APP.48786.

[11] C. Klahn, B. Leutenecker, M. Meboldt, "Design Strategies for the Process of Additive Manufacturing,", Procedia CIRP vol. 36 (2015) 230–235, https://doi.org/10.1016/J.PROCIR.2015.01.082.

[12] K. Xu, Y. Li, L. Chen, K. Tang, "Curved layer based process planning for multi-axis volume printing of freeform parts,", CAD Comput. Aided Des. vol. 114 (2019) 51–63, https://doi.org/10.1016/j.cad.2019.05.007.

[13] Y. Li, D. He, X. Wang, and K. Tang, "Geodesic Distance Field-based Curved Layer Volume Decomposition for Multi-Axis Support-free Printing," arXiv:2003.05938, Mar. 2020.

[14] M. Livesu, S. Ellero, J. Martínez, S. Lefebvre, M. Attene, "Fom 3D models to 3D prints: an overview of the processing pipeliner,", Comput. Graph. Forum vol. 36 (2) (2017) 537–564, https://doi.org/10.1111/cgf.13147.

[15] A.N. Ahsan, M.A. Habib, B. Khoda, "Resource based process planning for additive manufacturing,", CAD Comput. Aided Des. vol. 69 (2015) 112–125, https://doi.org/10.1016/J.CAD.2015.03.006.

[16] L. Luo, I. Baran, S. Rusinkiewicz, W. Matusik, "Chopper: Partitioning models into 3D-printable parts,", ACM Trans. Graph vol. 31 (6) (2012) https://doi.org/10.1145/2366145.2366148.

[17] K. Xu, L. Chen, K. Tang, "Support-Free Layered Process Planning Toward 3 + 2-Axis Additive Manufacturing,", IEEE Trans. Autom. Sci. Eng. vol. 16 (2) (2019) 838–850, https://doi.org/10.1109/TASE.2018.2867230.

[18] X. Xiao, S. Joshi, "Process planning for five-axis support free additive manufacturing,", Addit. Manuf. vol. 36 (2020), 101569 https://doi.org/10.1016/j.addma.2020.101569.

[19] Y. Murtezaoglu, D. Plakhotnik, M. Stautner, T. Vaneker, F.J.A.M. van Houten, "Geometry-based process planning for multi-axis support-free additive manufacturing,", Procedia CIRP vol. 78 (2018) 73–78, https://doi.org/10.1016/j.procir.2018.08.175.

[20] W. Gao, Y. Zhang, D.C. Nazzetta, K. Ramani, and R.J. Cipra, "RevoMaker: Enabling multi-directional and functionally-embedded 3D printing using a rotational cuboidal platform," UIST 2015 - Proceedings of the 28th Annual ACM Symposium on User Interface Software and Technology, pp. 437–446, 2015, doi: 10.1145/2807442.2807476.

[21] C. Wu, C. Dai, G. Fang, Y.J. Liu, C.C.L. Wang, "RoboFDM: A robotic system for support-free fabrication using FDM,", Proc. IEEE Int Conf. Robot Autom. (2017) 1175–1180, https://doi.org/10.1109/ICRA.2017.7989140.

[22] L. Wu, M. Jian, Y. Gao, Z. Liu, M. Yu, Y. Guan, "Global-optimization-based model decomposition for support-free multi-DOF 3D printing, " *SIGGRAPH Asia 2018 Posters, SA 2018* (2018) 4–5, https://doi.org/10.1145/3283289.3283352.

[23] E.A. Yu, J. Yeom, C.C. Tutum, E. Vouga, and R. Miikkulainen, "Evolutionary decomposition for 3D printing," GECCO 2017 - Proceedings of the 2017 Genetic and Evolutionary Computation Conference, vol. 8, pp. 1272–1279, Jul. 2017, doi: 10.1145/3071178.3071310.

[24] C. Wu, C. Dai, G. Fang, Y.J. Liu, C.C.L. Wang, "General support-effective decomposition for multi-directional 3D printing,", IEEE Trans. Autom. Sci. Eng. vol. 17 (2) (2020) 599–610, https://doi.org/10.1109/TASE.2019.2938219.

[25] B. Huang, S.B. Singamneni, "Curved layer adaptive slicing (CLAS) for fused deposition modelling,", Rapid Prototyp. J. vol. 21 (4) (2015) 354–367, https://doi.org/10.1108/RPJ-06-2013-0059.

[26] F. Hong, S. Hodges, C. Myant, and D.E. Boyle, "Open5x: Accessible 5-axis 3D printing and conformal slicing," Conference on Human Factors in Computing Systems - Proceedings, Apr. 2022, doi: 10.1145/3491101.3519782.

[27] G. Fang, S. Zhong, Z. Zhong, T. Zhang, X. Chen, C.C.L. Wang, "Reinforced FDM: multi-axis filament alignment with controlled anisotropic strength,", ACM Trans. Graph vol. 39 (6) (2020) 15, https://doi.org/10.1145/3414685.3417834.

[28] K. Hildebrand, B. Bickel, M. Alexa, "Orthogonal slicing for additive manufacturing,", in: Computers and Graphics, vol. 37, Pergamon,, 2013, pp. 669–675, https://doi.org/10.1016/j.cag.2013.05.011.

[29] Y. Guan, Y. Gao, L. Wu, K. Cui, J. Guo, and Z. Liu, "Multi-directional 3D printing with strength retention," SIGGRAPH Asia 2019 Posters, SA 2019, 2019, doi: 10.1145/3355056.3364559.

[30] D. Bi, F. Xie, K. Tang, "Generation of efficient iso-planar printing path for multi-axis FDM printing,", J. Manuf. Mater. Process. vol. 5 (2) (2021) 59, https://doi.org/10.3390/JMMP5020059.